

PAPER • OPEN ACCESS

Global gyrokinetic analysis of Wendelstein 7-X discharge: unveiling the importance of trapped-electron-mode and electron-temperature-gradient turbulence







To cite this article: Felix Wilms *et al* 2024 *Nucl. Fusion* **64** 096040

View the [article online](#) for updates and enhancements.

You may also like

- [Influence of sub-surface damage evolution on low-energy-plasma-driven deuterium permeation through tungsten](#)
Stefan Kapser, Martin Balden, Tiago Fiorini da Silva et al.
- [Summary of 21st joint EU-US transport task force workshop \(Leysin, September 5–8, 2016\)](#)
P. Mantica, C. Bourdelle, Y. Camenen et al.
- [Development of advanced high heat flux and plasma-facing materials](#)
Ch. Linsmeier, M. Rieth, J. Aktaa et al.

Global gyrokinetic analysis of Wendelstein 7-X discharge: unveiling the importance of trapped-electron-mode and electron-temperature-gradient turbulence

Felix Wilms^{1,*} , Alejandro Bañón Navarro¹ , Thomas Windisch², Sergey Bozhenkov² , Felix Warmer³ , Golo Fuchert², Oliver Ford², Daihong Zhang² , Torsten Stange², Frank Jenko¹  and the W7-X Team^a

¹ Max Planck Institute for Plasma Physics, Boltzmannstr. 2, 85748 Garching, Germany

² Max Planck Institute for Plasma Physics, Wendelsteinstr. 1, 17491 Greifswald, Germany

³ Eindhoven University of Technology, Eindhoven, Noord-Brabant, Netherlands

E-mail: felix.wilms@ipp.mpg.de

Received 2 February 2024, revised 3 May 2024

Accepted for publication 23 July 2024

Published 12 August 2024



CrossMark

Abstract

We present the first nonlinear, gyrokinetic, radially global simulation of a discharge of the Wendelstein 7-X-like stellarator, including kinetic electrons, an equilibrium radial electric field, as well as electromagnetic and collisional effects. By comparison against flux-tube and full-flux-surface simulations, we assess the impact of the equilibrium ExB-flow and flow shear on the stabilisation of turbulence. In contrast to the existing literature, we further provide substantial evidence for the turbulent electron heat flux being driven by trapped-electron-mode and electron-temperature-gradient turbulence in the core of the plasma. The former manifests as a hybrid together with ion-temperature-gradient turbulence and is primarily driven by the finite electron temperature gradient, which has largely been neglected in nonlinear stellarator simulations presented in the existing literature.

Keywords: Wendelstein 7-X, stellarator turbulence, gyrokinetic simulations

(Some figures may appear in colour only in the online journal)

^a See Grulke *et al* 2024 (<https://doi.org/10.1088/1741-4326/ad2f4d>) for the W7-X Team.

* Author to whom any correspondence should be addressed.



Original Content from this work may be used under the terms of the [Creative Commons Attribution 4.0 licence](https://creativecommons.org/licenses/by/4.0/). Any further distribution of this work must maintain attribution to the author(s) and the title of the work, journal citation and DOI.

1. Introduction

Due to the effectiveness in optimising neoclassical physics proven in [1], plasma turbulence has become the key driver of heat and particle transport in the plasma core of the Wendelstein 7-X (W7-X) stellarator [2].

The most prominent types of instabilities potentially driving turbulence in W7-X plasmas so far are the ion-temperature-gradient-mode (ITG), electron-temperature-gradient-mode (ETG) and trapped-electron-mode (TEM). In highly electromagnetic regimes of future experiments, instabilities such as kinetic-ballooning-modes, might become relevant [3, 4].

Although studies of ETG turbulence in stellarators date back as early as 2002 [5], its impact on transport processes in W7-X remains a subject of ongoing debate. It was argued in [6] that it should be negligible for W7-X, while it was concluded in [7] that ETGs could be the primary contributor to anomalous electron heat transport in certain experimental discharges. In contrast, extensive studies have focused on turbulence driven by ITG and TEM. It has been suggested that TEM turbulence is relatively weak in W7-X due to the ‘maximum- J ’ property, where most trapped electrons reside in regions of positive average magnetic field curvature [8–10]. However, it is worth mentioning that many, though not all, of those studies consider TEMs that are primarily driven by a finite density gradient rather than a finite electron temperature gradient (ETG). As a result, the most significant contributor to turbulence in the core of W7-X was hypothesised to be ITG, with TEMs only expected to be found in the edge region, if at all [2, 11].

Numerical studies on this subject, typically within the framework of gyrokinetic theory, have faced certain limitations. For instance, while works like [9, 12–15] consider experimental scenarios with realistic plasma dynamics, their simulations are limited to flux-tube (FT) domains. As such, effects like variations in the geometry perpendicular to the magnetic field lines and radial variation of the background profiles on the plasma dynamics cannot be captured accurately in this approach. Moreover, the full-flux-surface (FFS) simulations performed in [9] employed an adiabatic electron model, therefore leaving the effect of a radial electric field on TEM turbulence and ITG-TEM-hybrid scenarios unexplored.

Conversely, global nonlinear simulations, like those in [4, 16–20], often rely on analytical profiles or use simplifying assumptions, such as assuming an adiabatic electron model, neglecting collisions or neglecting electromagnetic effects. While each giving valuable insights into the behaviour of the underlying scenarios, the possibility of performing fully non-local simulations with realistic parameters is still unexplored.

We start lifting these constraints in this work by presenting a global simulation of experimental discharge parameters of W7-X using the GENE-3D code [16, 21]. The simulation employs a kinetic electron model, accounting for electromagnetic effects from magnetic flutter, collisions, and an equilibrium radial electric field. The only neglected effect is magnetic compression, which is expected to have a minor influence due to the overall low plasma- β in the scenario. To the best of the

authors’ knowledge, this simulation marks a pioneering effort of its kind for stellarators. We aim to compare the obtained heat flux levels against those from radially local FT and FFS simulations. This comparison will help assess the impact of the radial electric field and its shear while also expanding the scope of diagnostics available for analysing turbulence characteristics. Moreover, we challenge the prevailing hypothesis regarding trapped electron modes (TEM) being benign in the core of W7-X plasmas [2, 11]. Concurrently, we assess the influence of electron-scale turbulence, particularly driven by ETG modes, on the overall electron heat flux. Identifying and differentiating between these various turbulence types is highly significant, considering they demand distinct mitigation strategies [22, 23].

The rest of this paper is structured as follows: section 2 introduces the details of the experimental discharge considered throughout this work. In section 3, the heat fluxes predicted by simulations with different computational domains are compared and the effect of the radial electric field on the overall transport is discussed. Subsequently, the predicted heat fluxes are compared against those derived from a power balance analysis. The characteristics of ion-scale turbulence in the discharge’s core region are investigated in section 4, showing evidence for TEM contributing significantly to the total transport. In section 5, the contribution of ETG turbulence on the electron heat flux is explored, and the reasons for its varying strength at different radial positions are discussed. Finally, in section 6, we justify the significance of these results in the experimental context, even though they may not align perfectly with power balance.

2. Details of the discharge

In the rest of this work, we consider an experimental Electron-Cyclotron-Resonance-Heated (ECRH) discharge of W7-X. Specifically, our focus is on the W7-X programme 20181016.037 [9], for which the corresponding time traces can be found in figure 1. For our purposes, the discharge phase of $t=4\text{--}5\text{ s}$ is particularly well-suited. It can be considered a representative scenario for gas-fuelled standard discharges within W7-X. The relevant background density and temperature profiles are shown in figure 2, together with the equilibrium radial electric field calculated by the neoclassical transport code DKES [24]. One thing to note is that $T_i \geq T_e$ for some positions beyond $\rho_{\text{tor}} \approx 0.5$. This contradicts the expectations for a plasma solely heated by ECRH, as the ions are only heated through equipartition with the electrons. However, this discrepancy is of minor concern to us. To analyse turbulent dynamics beyond comparing the different simulation models, we largely focus on the region $\rho_{\text{tor}} \leq 0.5$, as will become clear in subsequent discussions.

3. Comparison of computational domains

As a first step, we compare the heat fluxes predicted by FT, FFS and radially global simulations, as each model offers distinct diagnostic capabilities. For instance, while flux-surface

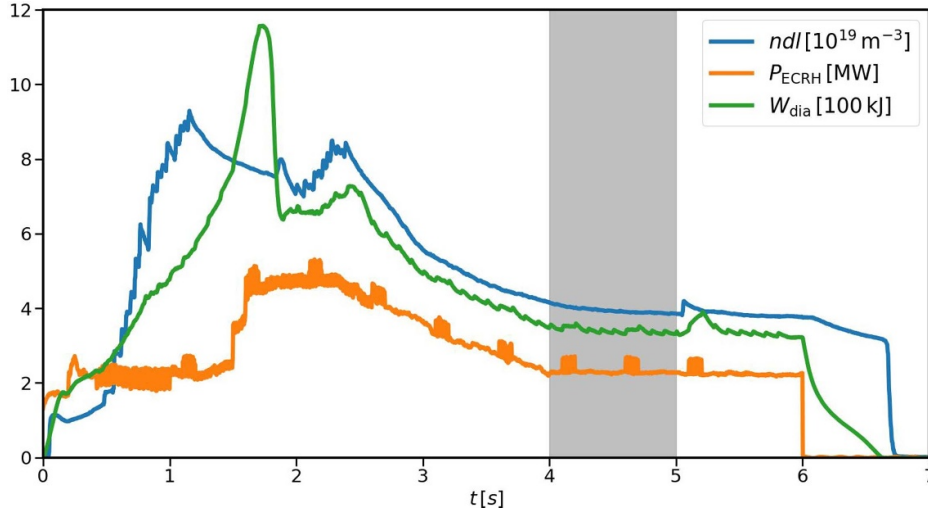


Figure 1. Time traces of the line-integrated density (blue), ECRH heating power (orange) and diamagnetic energy (green) of the W7-X programme 20181016.037. The area marked in grey at $t = 4\text{--}5$ s corresponds to the shot phase considered in this investigation.

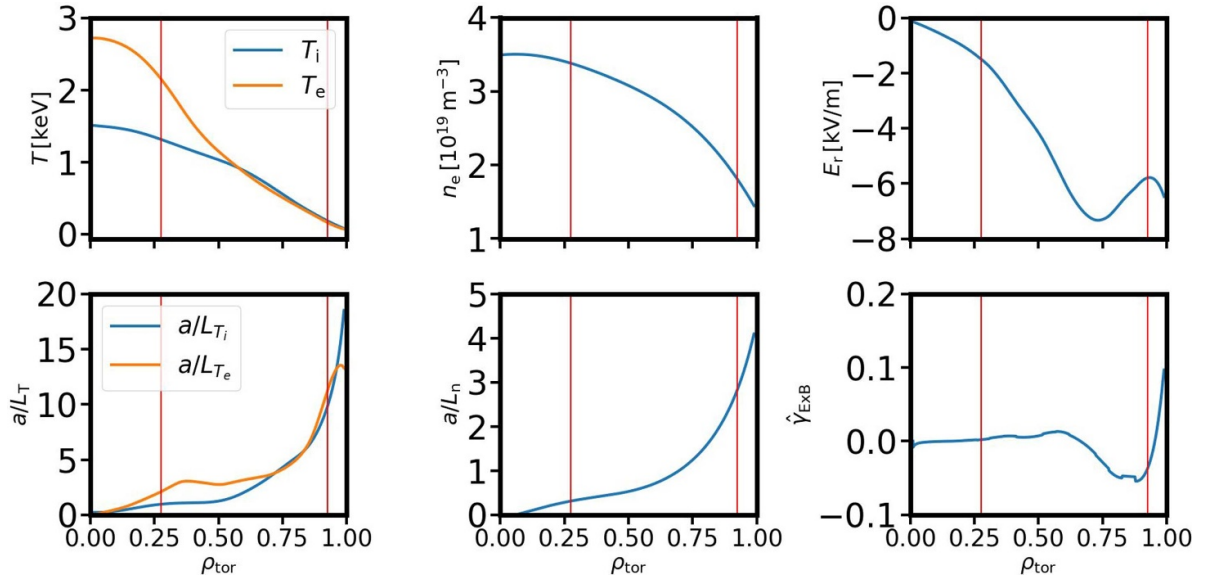


Figure 2. Density, temperature and radial electric field profiles corresponding to the grey area in figure 1. Top: profiles, bottom: corresponding (normalised) gradients. Bottom right: normalised flow-shear rate, defined in equation (4). The red lines indicate the limits of the domain simulated with GENE-3D.

and global simulations can provide the spatial patterns of turbulence across the entire surface, FT simulations can isolate single toroidal modes in linear simulations, which will prove valuable in the subsequent analysis.

The FT simulations presented in this work were performed with the GENE code, whereas FFS and radially global simulations were performed with GENE-3D. While detailed discussions about their algorithms can be found in [25, 26] and [16, 21], respectively, we note here that both codes use the Clebsch-type spatial coordinates

$$\begin{aligned} x &= a \rho_{\text{tor}} \\ y &= \sigma_{B_p} C_y \alpha = \sigma_{B_p} C_y (\theta^* / \iota(x) - \phi) \\ z &= \sigma_{B_p} \theta^*. \end{aligned} \quad (1)$$

Here, $\rho_{\text{tor}} = \sqrt{\Phi_{\text{tor}} / \Phi_{\text{edge}}}$ is used as a radial coordinate, where Φ_{tor} is the toroidal flux and Φ_{edge} its value at the last closed flux-surface. The binormal coordinate y is based on the field line label α at a fixed flux-surface, where $\iota(x)$ is the rotational transform, and θ^* and ϕ are the poloidal and toroidal PEST angles [27], respectively. The quantity σ_{B_p} is the sign of the poloidal magnetic field and ensures that the parallel coordinate z is always in the direction of the background magnetic field \mathbf{B}_0 . Furthermore, the effective minor radius $a = \sqrt{\Phi_{\text{edge}} / (\pi B_{\text{ref}})}$ is defined via the toroidal magnetic flux at the edge, as well as the magnetic field strength B_{ref} at the axis and the variable C_y is defined via the reference position x_0 as $C_y = x_0 |\iota(x_0)|$. We use the velocity v_{\parallel} parallel to the magnetic field and the magnetic moment $\mu = m_{\sigma} v_{\perp}^2 / (2B_0)$

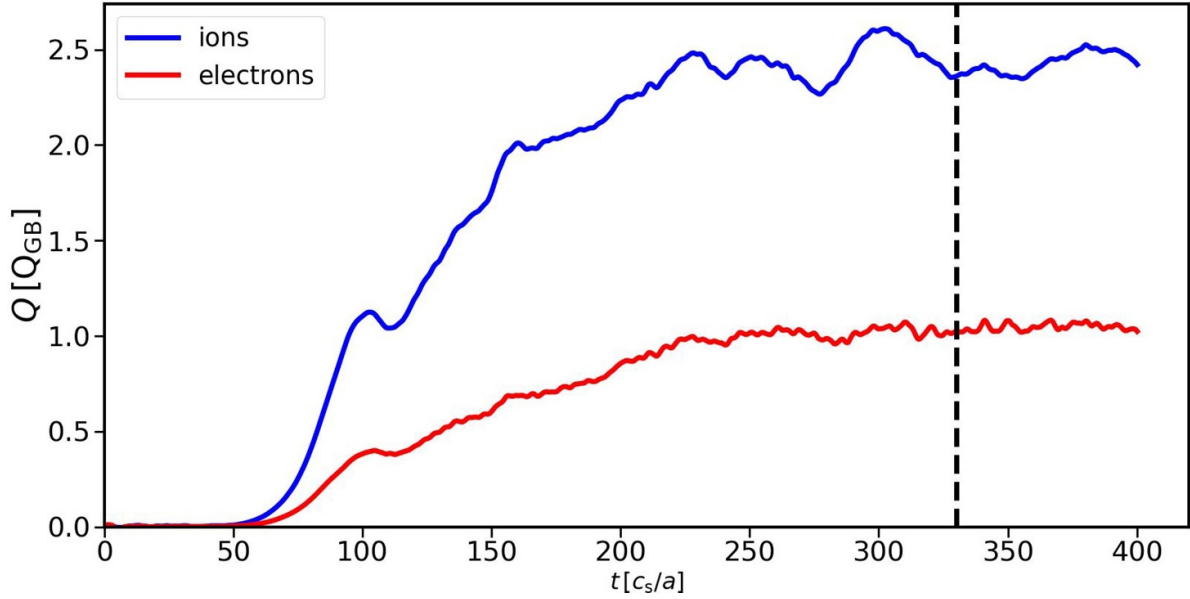


Figure 3. Time trace of the volume-averaged heat flux of the global simulation. The black dashed line indicates the starting point for computing averaged quantities.

as velocity space coordinates for each species σ . Finally, one can also show that the equilibrium magnetic field \mathbf{B}_0 can be written as

$$\mathbf{B}_0 = B_{\text{ref}} \hat{C}(x) \nabla x \times \nabla y, \quad (2)$$

where $\hat{C} = x|\iota(x)|/(x_0|\iota(x_0)|)$.

In the following, we consider the radial domain $\rho_{\text{tor}} \in [0.275, 0.925]$, which accounts for roughly 65% of the entire inner plasma volume. The global simulation performed with GENE-3D uses a resolution of $(325, 256, 126, 64, 16)$ points in the $(x, y, z, v_{\parallel}, \mu)$ -directions, respectively. The corresponding numerical box dimensions are $(L_x, L_y, L_{v_{\parallel}}, L_{\mu}) = (259.437, \rho_s, 265.472, \rho_s, 3.45, v_{\text{th},\sigma}, 11.9, T_{\sigma}(x_0)/B_{\text{ref}})$, covering one fifth of the surface in the binormal direction by utilising the five-fold symmetry of W7-X. The spatial box is given in units of the ion sound Larmor radius $\rho_s = c_s/\Omega_p$, which is defined via the sound velocity $c_s = \sqrt{T_e(x_0)/m_p}$ and the proton Larmor frequency $\Omega_p = eB_{\text{ref}}/(m_p c)$. The parallel velocity box is given in units of the thermal velocity $v_{\text{th},\sigma} = \sqrt{2T_{\sigma}(x_0)/m_{\sigma}}$ of species σ . Using approximately 2.8 million core hours on the MPCDF cluster Raven, the simulated plasma is saturated based on the time traces of the volume-averaged heat fluxes illustrated in figure 3. To the author's knowledge, this simulation marks the first instance of a global gyrokinetic simulation conducted with experimental discharge parameters from W7-X, incorporating kinetic electrons and accounting for electromagnetic effects. The heat flux profiles are then compared with those obtained by radially local simulations, carried out at the radial positions $\rho_{\text{tor}} = [0.4, 0.5, 0.6, 0.7, 0.8]$. The comparison is shown in figure 4. The FFS simulations are also performed, covering one fifth of the respective surface. In these simulations, numerical boxes

of $(L_x, L_{v_{\parallel}}, L_{\mu}) = (225 \rho_s, 3 v_{\text{th},\sigma}(x_0), 9 T_{0,\sigma}(x_0)/B_{\text{ref}})$ and resolutions of $(n_x, n_y, n_z, n_{v_{\parallel}}, n_{\mu}) = (225, 256, 128, 32, 9)$ were sufficient for most cases. However, the velocity space had to be adapted to $(L_{v_{\parallel}}, L_{\mu}, n_{v_{\parallel}}, n_{\mu}) = (6, 12, 64, 12)$ for the simulations at $\rho_{\text{tor}} = 0.4$ and 0.5 . Unless stated otherwise, a finite equilibrium ExB-flow corresponding to the local value of the nominal radial electric field $E_r = -d\phi_0(x)/dx$ is included in the simulations. Both types of simulations assumed zero-Dirichlet boundary conditions for the radial domain, necessitating the use of a Krook damping operator in 5% of the grid points at each of the two boundaries for numerical stability. In addition, numerical heat and particle sources with amplitudes of $\kappa_H = 0.02$ and $\kappa_P = 0.02$ were used to avoid relaxation of the background profiles. Furthermore, numerical hyper-diffusion with amplitudes $(\eta_x, \eta_y, \eta_z) = (0.5, 0.5, 27)$ for the global and $(\eta_x, \eta_y, \eta_z) = (0.5, 0.2, 27)$ for the radially local simulations. For details on the implementation of the numerical damping schemes, the reader is referred to [16].

Four FT simulations were performed at $\alpha = [0, 0.25, 0.5, 0.75]\pi/5$ using GENE instead of GENE-3D at each radial position. Since it uses a Fourier representation in the binormal direction, the numerical boxes were chosen to be $(k_{y,\text{min}}, L_{v_{\parallel}}, L_{\mu}) = (0.05 \rho_s^{-1}, 3 v_{\text{th},\sigma}(x_0), 9 T_{0,\sigma}(x_0)/B_{\text{ref}})$ with $k_{x,\text{min}} = 2\pi/L_x$ and $k_{y,\text{min}} = 2\pi/L_y$. Resolutions of $(n_{k_x}, n_{k_y}, n_z, n_{v_{\parallel}}, n_{\mu}) = (128, 64, 128, 32, 9)$ were found to be sufficient. The radial box sizes are selected to be approximately $L_x \approx 225 \rho_s$ and are adjusted according to constraints imposed by the magnetic shear $\hat{s}(x_0) = -x_0 d\ln(\iota)/dx|_{x=x_0}$ [28]. In cases where the shear becomes too small, periodic boundary conditions in the z direction are assumed. In addition, hyper-diffusion with amplitudes $(\eta_{k_x}, \eta_{k_y}, \eta_z) = (0.0, 0.1, 27)$ were used.

In figure 4, we observe a reasonable agreement in heat flux levels between the local and global simulations within the

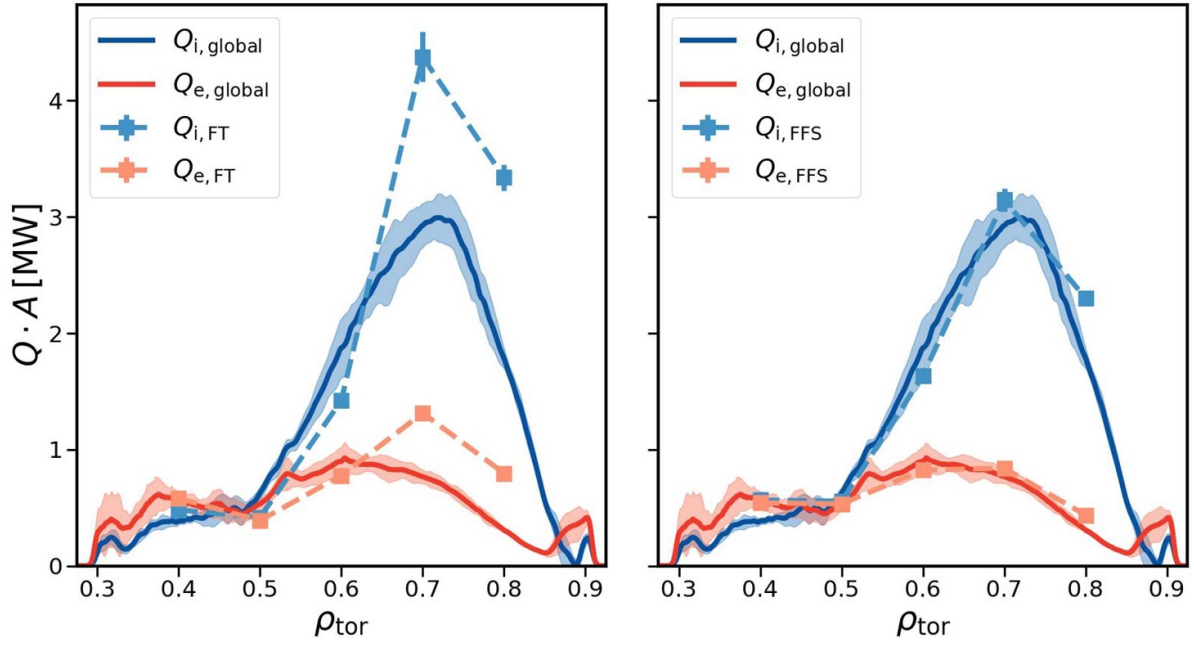


Figure 4. Comparison of the radial heat flux profile obtained from the global simulation with those obtained by flux-tube (left) and full-flux-surface (right) simulations. Shaded regions indicate standard deviation in time of the global simulation.

core. However, significant discrepancies arise between the FT and global results in the outer region, reaching up to a factor of two difference at $\rho_{\text{tor}} = 0.8$. On the contrary, FFS and global simulations match better, displaying a relative error of approximately 30% at the same position. The discrepancies in figure 4 can partly be attributed to how each simulation model handles the external radial electric field. FT simulations can eliminate a constant radial electric field by coordinate transformation into a reference frame that rotates with the flow velocity, unlike in FFS simulations, as the binormal variation of the magnetic field breaks rotational invariance. Global simulations naturally account for the radial variation of the electric field, therefore including a sheared flow in the system, which is known to stabilise turbulence. However, local simulations can approximate ExB-flow shear by linearising the normalised flow velocity around the respective flux-surface:

$$\hat{v}_{E_0} = -\frac{\hat{E}_r(x)}{\hat{C}(x)} \approx -\left(\frac{\hat{E}_r(x_0)}{\hat{C}(x_0)} - \hat{\gamma}_{\text{ExB}}(x_0)(\hat{x} - \hat{x}_0)\right). \quad (3)$$

Here, $\hat{\gamma}_{\text{ExB}}$ represents the normalised shearing rate given by

$$\begin{aligned} \hat{\gamma}_{\text{ExB}}(x_0) &\equiv -\frac{d}{d\hat{x}} \left(\frac{\hat{E}_r(x)}{\hat{C}(x)} \right) \Big|_{x=x_0} \\ &= -\left[\frac{d\hat{E}_r}{d\hat{x}} - \frac{\hat{E}_r}{\hat{x}}(1 - \hat{s}) \right] \Big|_{x=x_0}, \end{aligned} \quad (4)$$

with $\hat{x} = \rho_s \rho_{\text{tor}}$ and $\hat{E}_r = T_e(x_0) E_r / (ea)$.

Incorporating the sheared ExB-flow in the radially local simulations notably influences the outer radial region, as depicted in figure 5. Given the relatively low shear rate in

the inner region, it is understandable that the transport levels remain largely unaffected, although agreement between local and global simulations becomes worse at $\rho_{\text{tor}} = 0.6$, something that is left to be explored in the future. Repeating the FFS simulation at $\rho_{\text{tor}} = 0.8$, excluding the constant equilibrium ExB-flow shows that the constant local radial electric field does not notably influence the transport levels at this position, as can be seen in table 1. However, when factoring in the flow shear, there is a reduction of about 20%–25% in heat fluxes for both FT and FFS simulations. With this, the ion heat flux calculated by the latter is reduced to a level agreeing with the global results within error bars. This underscores the significant impact of sheared equilibrium ExB-flows on turbulence in stellarators, emphasising the necessity to consider these dynamics in gyrokinetic simulations. Such considerations are especially crucial in advanced scenarios, like those involving pellet fuelling, where an even more pronounced radial variation in the electric field can be found [9]. In addition, we see from figures 4 and 5 that the three simulation models agree well with each other in the core of the plasma, allowing us to use all of them for the subsequent analysis of ion-scale turbulence found in this scenario.

4. Analysis of ion-scale turbulence in the core

Having compared the discharge's heat fluxes levels computed by the different simulation models, we focus on the detailed analysis of its turbulent plasma dynamics. To this end, we compare the global heat flux profiles predicted by GENE-3D against the anomalous heat fluxes calculated with the NTSS code [29] as the difference between total and neoclassical

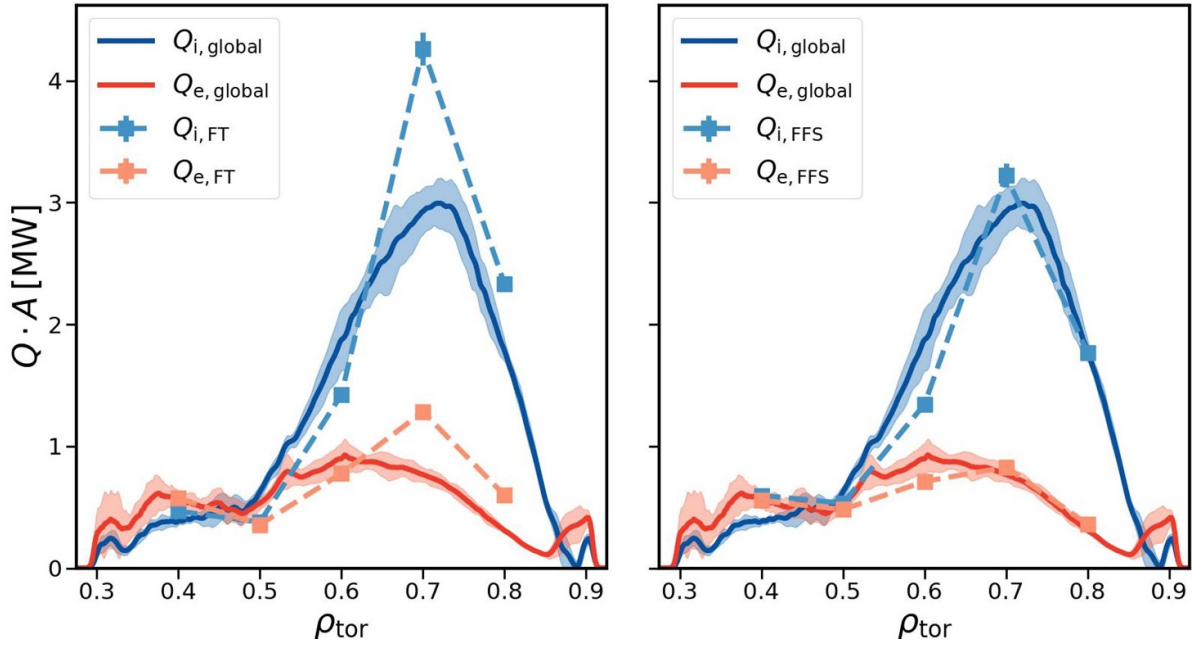


Figure 5. Same as figure 4 but linearised flow shear was added for the radially local simulations.

Table 1. Ion and electron heat fluxes at $\rho_{\text{tor}} = 0.8$ as predicted by different models.

	$Q_{\text{ions}} \cdot A$ (MW)	$Q_{\text{electrons}} \cdot A$ (MW)
Flux-tube	3.34 ± 0.11	0.80 ± 0.02
Flux-tube (with $\hat{\gamma}_{\text{ExB}}$)	2.34 ± 0.04	0.60 ± 0.01
Flux-surface (no E_r)	2.32 ± 0.06	0.44 ± 0.01
Flux-surface (with E_r)	2.30 ± 0.05	0.44 ± 0.01
Flux-surface (with E_r & $\hat{\gamma}_{\text{ExB}}$)	1.77 ± 0.03	0.36 ± 0.01
Global	1.77 ± 0.08	0.30 ± 0.02

heat flux obtained with DKES in figure 6. The comparison between the turbulent heat fluxes derived from power balance and GENE-3D indicates a good agreement in ion heat flux up to $\rho_{\text{tor}} = 0.5$. Beyond that, GENE-3D predicts heat fluxes well above those given by NTSS, even exceeding the total ECRH heating power shown in figure 1. In contrast, the electron heat flux is below the power balance prediction over the entire radial domain. Therefore, we primarily consider the region with $\rho_{\text{tor}} \leq 0.5$ for in-depth investigations of turbulence characteristics.

It was proposed by [2, 11] that ITG would primarily govern the plasma core's turbulence, while any presence of TEMs would likely manifest in the plasma edge. However, the findings depicted in figure 6, both from GENE-3D and NTSS analyses, suggest that this hypothesis might only hold partly true. As supported by [30], 'pure' ITG turbulence can be expected to drive mainly ion heat flux with only little impact on the electron channel. In contrast, GENE-3D and NTSS predictions predict either $Q_e \geq Q_i$ or $Q_e \gg Q_i$ within the core, which can also be anticipated if direct plasma heating is only applied to the electrons. Given that

electromagnetic turbulence should be subdominant for the plasma- β of the discharge, TEM turbulence emerges as a likely candidate.

We have selected the flux-surface at $\rho_{\text{tor}} = 0.4$ as representative for detailed analysis within the inner plasma core. Figure 7 shows the spatial heat flux distribution for electron and ion channels along the parallel coordinate z and the field-line label α . Notably, the ion heat flux exhibits a predominant single central peak, contrasting the electron heat flux, which displays multiple maxima along z at fixed α . The distinction becomes notably clearer when comparing the parallel structure at $\alpha = 0$ from FT simulations with both the magnetic field structure and the binormal magnetic field curvature $\mathcal{K}_y = -(\mathbf{B}_0 \times \nabla|\mathbf{B}_0|) \cdot \mathbf{e}_y$, shown in figure 8, where \mathbf{e}_y is the covariant binormal basis vector. The ion heat flux seems to peak where \mathcal{K}_y is the most negative, which is typical for toroidal ITG [31, 32]. Conversely, the electron heat flux shows a more pronounced influence from the magnetic well structure. This is evident as the electron heat flux displays a local minimum at $z = 0$, even though the curvature has a local minimum. Furthermore, its local maxima coincide closely with the magnetic wells' minima, which is typical for trapped-electron modes [31]. The combination of both structural features in the different particle channels suggest the presence of a hybrid ITG-TEM mode, further supported by the linear FT simulations depicted in figure 9. In there, all the analysed modes exhibit a positive frequency, therefore propagating in the ion-diamagnetic direction. However, one can observe that ions and electrons have positive and comparable contributions to the linear growth rates [33] and therefore both drive the respective instability. It was shown in [31] that in the case of pure ITG or TEM the instabilities were primarily driven by the ions and the electrons, respectively, which is not the

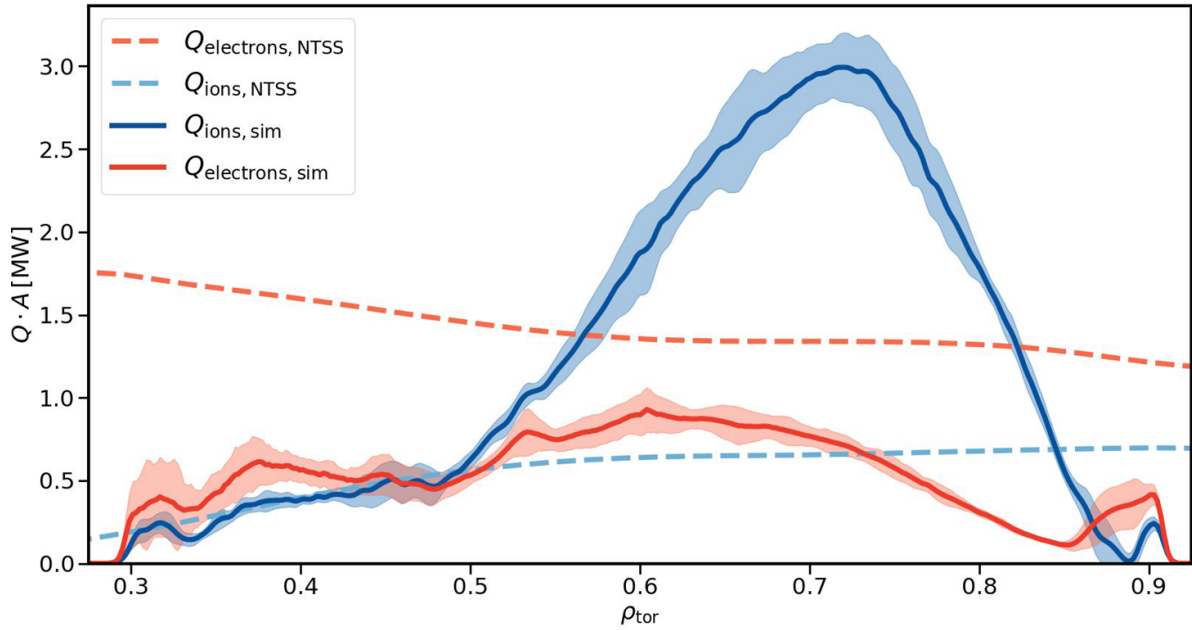


Figure 6. Comparison of the radial heat flux profile obtained from the global simulation with the anomalous heat fluxes derived from power balance using NTSS. Shaded regions indicate standard deviation in time of the global simulation.

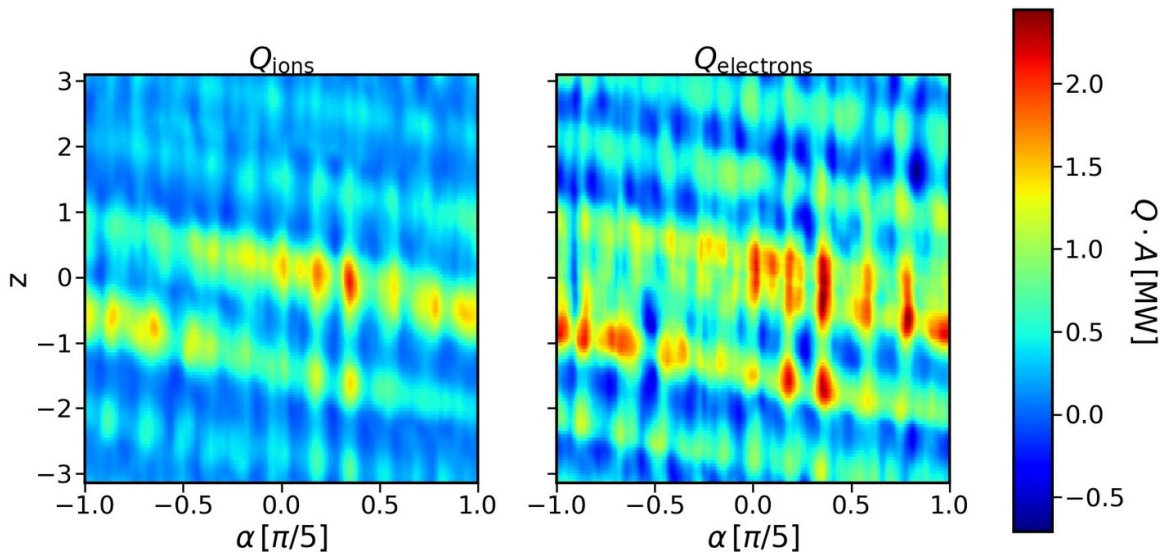


Figure 7. Electron and ion heat fluxes at $\rho_{\text{tor}} = 0.4$, obtained by the global simulation, as a function of the parallel coordinate z and the field-line label α .

case for the instabilities considered in figure 9, as all of them have comparable growth rate contributions coming from ions and electrons. Furthermore, one can rule out the presence of ion-driven trapped-electron-modes [34], which were shown in the same publication to feed mainly on the free energy of the ions. As a consequence, it stands to reason that the linear modes presented here can be characterised as ITG-TEM hybrid modes, which is further justified when considering the quasilinear heat flux ratios that are shown in figure 9 as well. It was argued in [35] that comparable heat flux estimates indicate a strong coupling between both particle channels and indicate the presence of hybrid ITG-TEM modes, further supporting

our hypothesis. Furthermore, one can notice in the growth rate spectrum that there is no decrease within the scanned wavenumber range. However, it becomes evident that these small-scale modes do not significantly contribute to the nonlinear transport, as the corresponding nonlinear heat flux spectra shown in figure 10, are primarily dominated by wavenumbers up to $k_y \rho_s \approx 1$.

We finalise this investigation by assessing the impact of each temperature gradient on the transport channels. While this approach is not fully rigorous, it provides valuable insights into the contributions of various turbulence types to the overall system dynamics. Table 2 shows that excluding the normalised

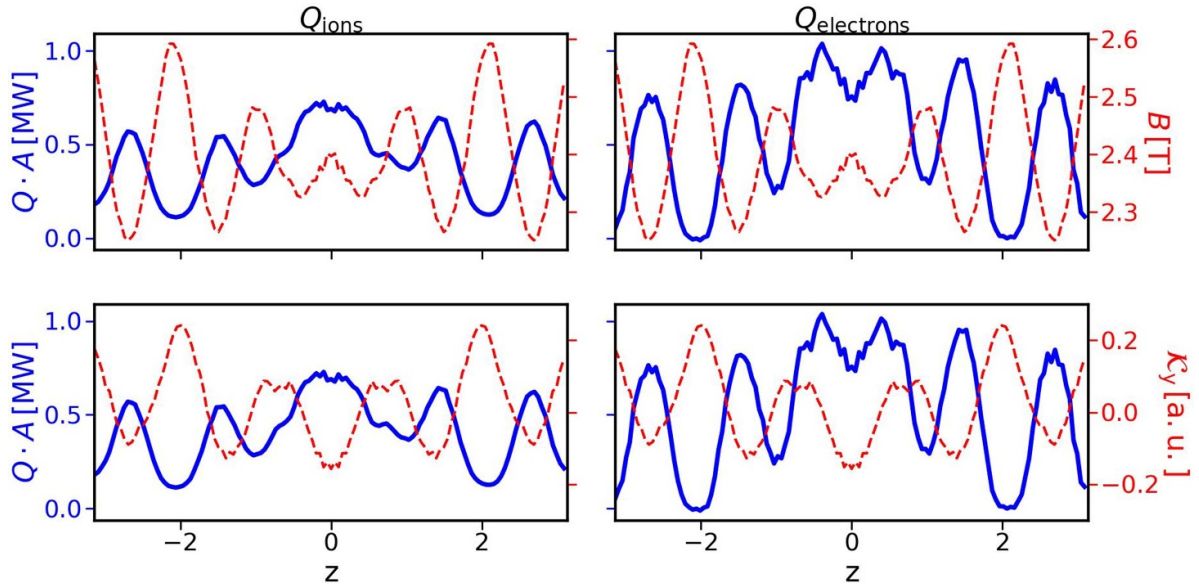


Figure 8. Blue: parallel ion (left) and electron (right) heat flux structures for the flux-tube simulation at $\rho_{\text{tor}} = 0.4$, $\alpha = 0$ with nominal parameters; red: parallel structure of the equilibrium magnetic field strength (top) and the curvature-drive term \mathcal{K}_y (bottom).

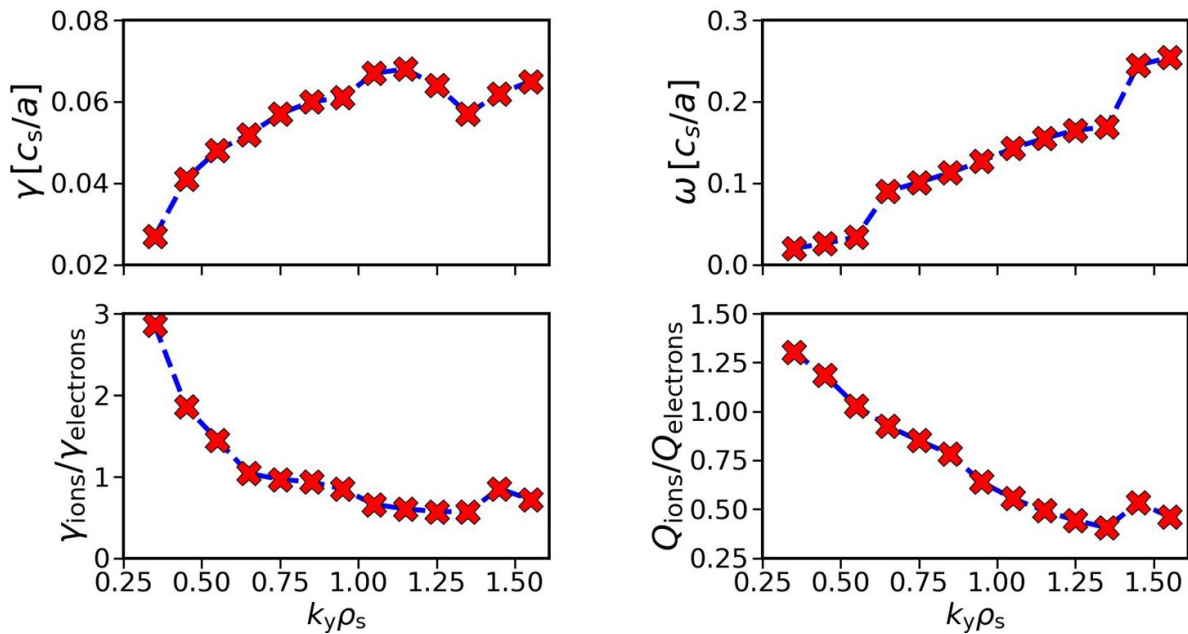


Figure 9. Linear flux-tube wavenumber-scan for the bean-shaped flux-tube at $\rho_{\text{tor}} = 0.4$; top left: growth rates, top right: mode frequencies, bottom left: ratio of ion and electron contributions to the growth rates, bottom right: quasilinear estimates of the ion-to-electron heat flux ratio.

ETG, compared to the nominal parameters, has a negligible impact on the ion heat flux. It remains similar to the nominal case within error bars. Conversely, in this scenario, the electron heat flux reduces by approximately 85%, leading to the ion channel dominating the total transport. As shown in figure 11, the modified ion heat flux exhibits a ballooning-type structure along the magnetic field lines, including significantly stronger contributions around $z=0$ in contrast to that with nominal gradients. Comparable structures were documented in [9] for a case categorised as ITG-driven, which we conclude is also

the dominant type of turbulence if the ETG is neglected. The fact that the electron heat flux reduces significantly and one observes a transition to a different type of turbulence underlines the significance of this particular branch of TEM compared to those primarily driven by an electron density gradient, which have received more attention in existing literature [8, 9, 36, 37].

In summation, evidence derived from the power balance, heat flux structure, and linear FT analysis within this section collectively suggests that in contrast to the proposition

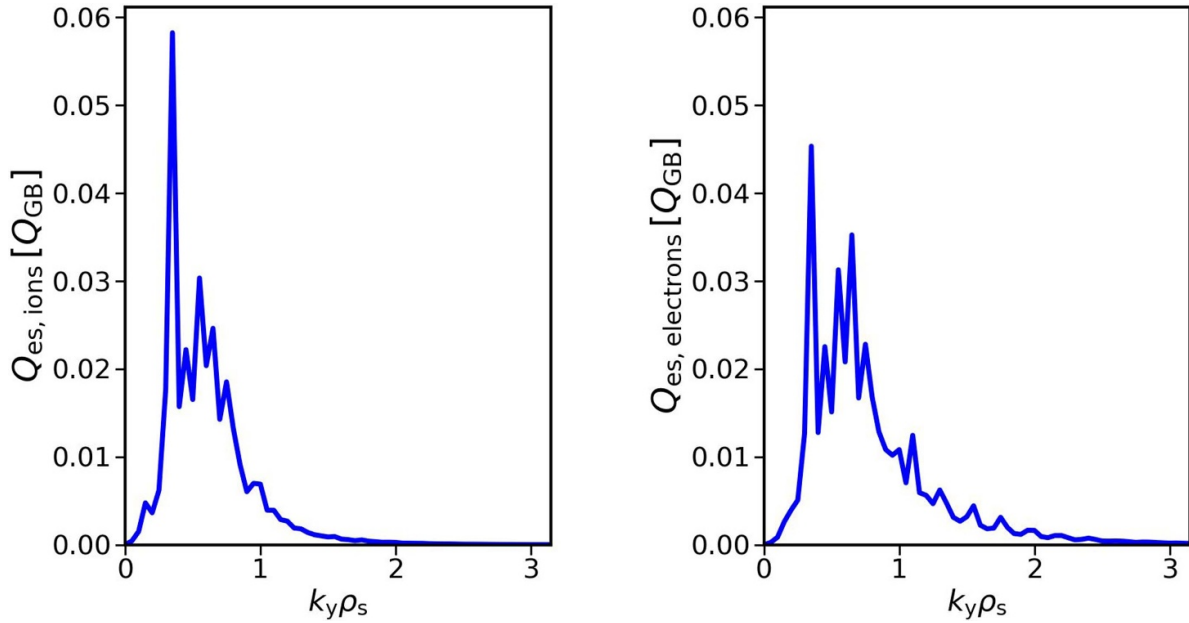


Figure 10. Nonlinear heat flux spectra for the bean-shaped flux-tube at $\rho_{\text{tor}} = 0.4$; left: ion heat flux, right: electron heat flux.

Table 2. Heat fluxes of flux-tube simulations at $\rho_{\text{tor}} = 0.4$, $\alpha = 0$, for nominal parameters and either electron or ion temperature gradient set to zero.

Case	$Q_{\text{ions}} \cdot A$ (MW)	$Q_{\text{electrons}} \cdot A$ (MW)
Nominal	0.42 ± 0.05	0.49 ± 0.07
$a/L_{T_e} = 0$	0.49 ± 0.06	0.07 ± 0.01
$a/L_{T_i} = 0$	0.01 ± 0.00	0.18 ± 0.01

outlined in [2, 11], TEM turbulence seems to be present within the core of the gas-fuelled discharge in W7-X, at least for the specific discharge under consideration. However, the applicability of this observation for general experimental scenarios requires further exploration, a task reserved for future investigations.

5. Impact of ETG turbulence

As shown in figure 6, there is a strong alignment between the anticipated anomalous ion transport derived from power balance analysis and the one computed using GENE-3D within the core region. However, the predicted electron transport remains notably lower. It is crucial to notice that our focus has predominantly been on turbulence at ion lengthscales thus far. Consequently, the remaining contribution to the electron flux might be driven by ETG turbulence, which has not yet been captured in our simulations.

To this end, we perform additional FT simulations using an adiabatic ion model. We consider the FTs at $\alpha = [0, 0.25, 0.5, 0.75]\pi/5$ for $\rho_{\text{tor}} = [0.3, 0.4, 0.5, 0.6, 0.7, 0.8, 0.9]$. The numerical resolution and box sizes remain the same as those used in the ion-scale

simulations in section 3, with the exception being the use of the electron sound Larmor radius ρ_e for normalisation instead of the ion sound Larmor radius ρ_s .

The resulting fluxes, measured in megawatts, are averaged over the field-line labels and added to the ion-scale electron heat flux predicted by GENE-3D via linear interpolation in the radial coordinate. Figure 12 shows the updated global flux profiles. In there, we observe that the contribution from electron-scale turbulence is negligible in the outer radial region. Nevertheless, ETG turbulence seems to be responsible for more than 50% of the turbulent electron heat flux within the plasma core. Our findings corroborate those in [7], which identified ETG turbulence as a possible primary driver for electron heat transport in the core for certain experimental scenarios. However, the electron-scale contribution to their discharges was identified as even stronger than for the present case.

In order to understand why electron-scale transport is negligible in the edge region in comparison with that in the core region, one has to consider several possible factors. As illustrated in figure 13, the heat flux exhibits a near-constant behaviour despite variations in the field-line label. Hence, the selection of the FT or subsequent averaging procedures should be negligible for the remaining discussion. Previous investigations into ETG dynamics in Wendelstein 7-AS [5] and similar simulations conducted in tokamaks [25] have suggested that collisionality and plasma- β exert only minor influence on the electron-scale transport levels. However, the same studies indicated that the electron-to-ion temperature ratio $\tau = T_e/T_i$ and the normalised Debye length $\lambda_{\text{De}} = \lambda_{\text{De}}/\rho_e = \sqrt{B_{\text{ref}}^2/(4\pi c^2 m_e n_e(x))}$ notably affect ETG turbulence. As depicted in figure 14, the reduction in τ does not seem to account for the decreasing contribution of ETG to the

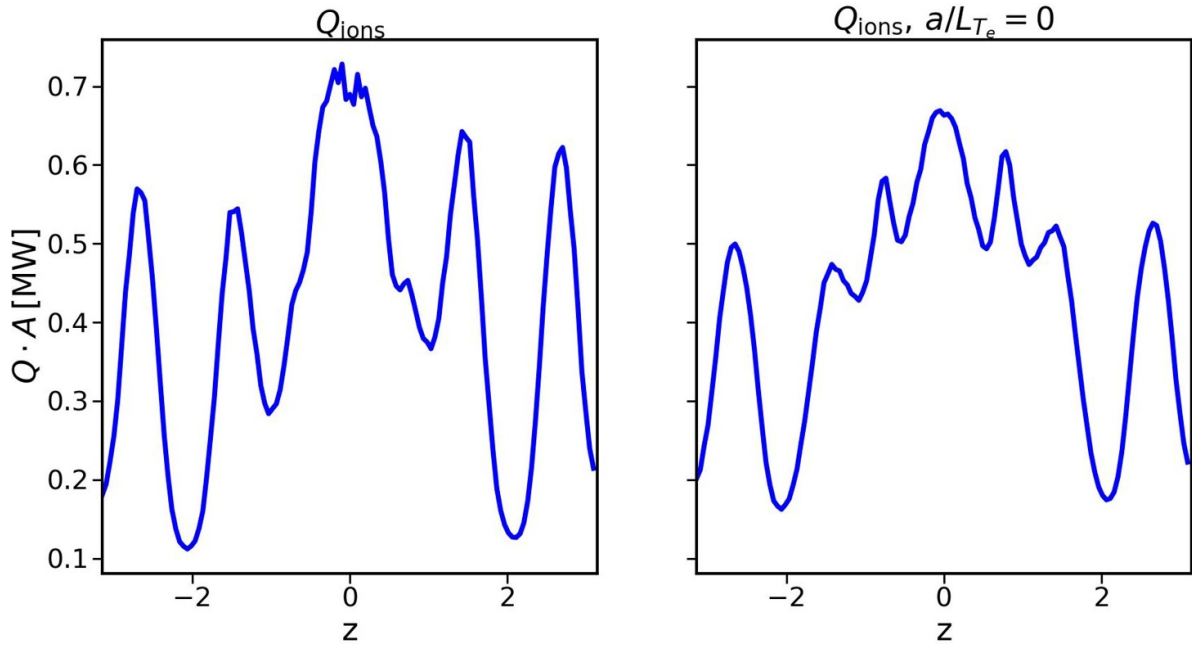


Figure 11. Left: parallel ion heat flux structure for the flux-tube simulation with nominal parameters; right: parallel ion heat flux structure for the flux-tube simulation with $a/L_{T_e} = 0$.

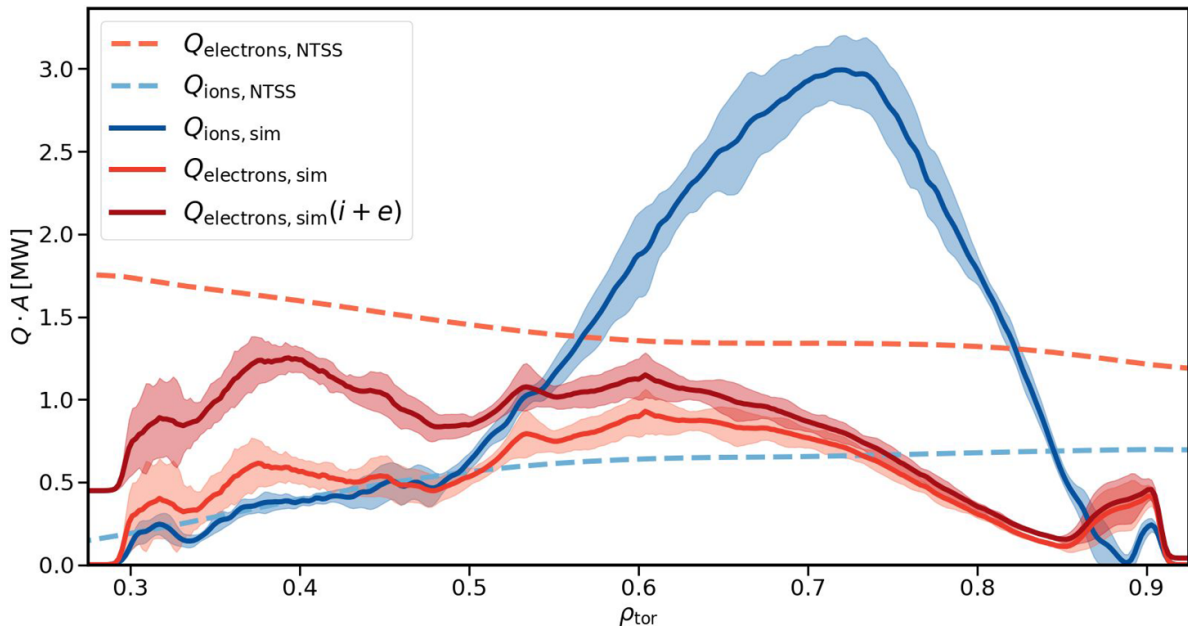


Figure 12. Comparison of the radial heat flux profile with the anomalous heat fluxes derived from power balance analysis. The dark red line shows the sum of electron heat fluxes of (separated) ion- and electron-scale simulations. Shaded regions indicate standard deviation in time of the global simulation.

overall flux, as a decrease in τ theoretically implies destabilisation toward the outer region [5]. Beyond the variation in τ , figure 14 shows that $\hat{\lambda}_{De}$ increases towards the edge, which is thought to have a stabilising influence on ETG turbulence. We repeated the FT simulations while artificially setting $\hat{\lambda}_{De} = 0$ to investigate this. The results presented in figure 15 indicate that the stabilisation attributed to Debye shielding falls short in explaining the radial changes in electron-scale transport.

Notably, the difference between both models diminishes significantly towards the edge. In addition to geometric factors like magnetic field curvature, the normalised gradient ratio $\eta_e = L_n/L_{T_e}$ is known to influence transport significantly, as a decrease tends to stabilise ETG turbulence. This effect was proposed to explain the low electron-scale transport in the outer region of a discharge discussed in [6]. If this were the primary driver, neglecting the density gradient should

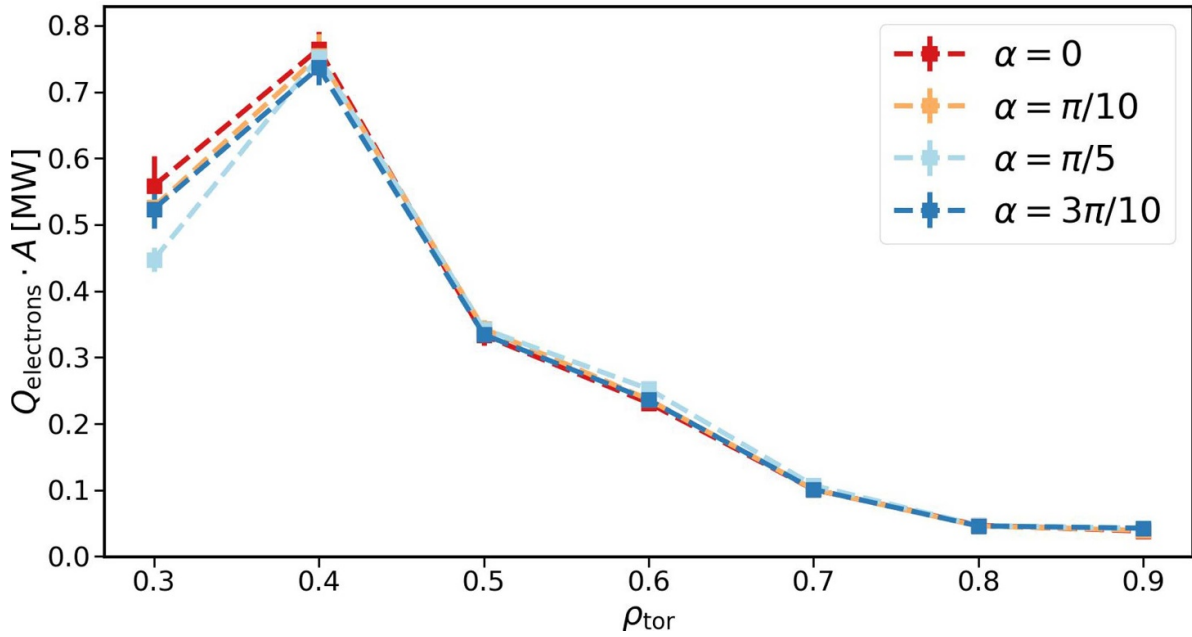


Figure 13. Electron heat fluxes obtained by local ETG simulations as a function of the radial coordinate for different field-line labels.

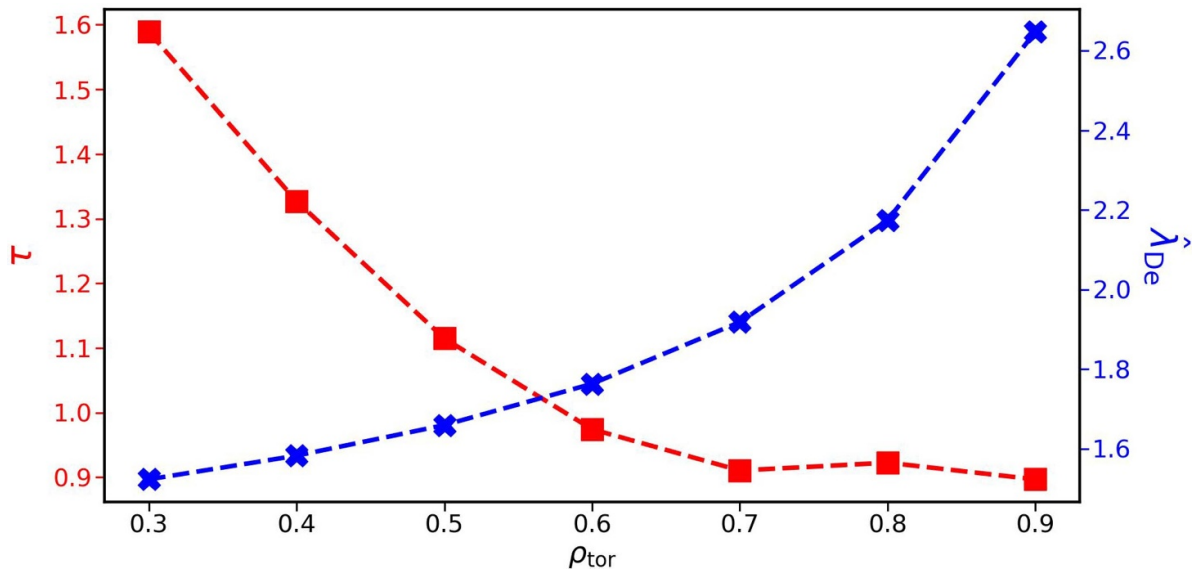


Figure 14. Variation of the temperature ratio $\tau = T_e/T_i$ (red) and the normalised Debye length (blue) as a function of the radial coordinate.

logically yield a radial flux profile that increases towards the edge together with the normalised ETG, which drives ETG.

However, while the decrease of η_e along the radial direction aligns with the notion of stabilisation through the density gradient, figure 16 reveals that eliminating the density gradient still leads to a decrease in heat flux towards the edge.

Having eliminated all other options, we conclude that ETG transport is not stiff enough, meaning that the heat flux does not increase sufficiently fast enough with increasing background drive, to compensate for the decrease in

density and temperature towards the outer regions. To confirm this, we show the radial profile of the normalised electron heat flux and the Gyrobohm scaling factor profile in figure 17. In there, we see that the normalised heat flux notably increases by more than an order of magnitude towards the edge, coinciding with the growing normalised ETG. However, the Gyrobohm scaling factor drops rapidly over two orders of magnitude from the core to the edge. Consequently, it becomes evident that the normalised flux fails to grow fast enough with the background drive. As a result, the product of these two factors decreases as the radial position increases.

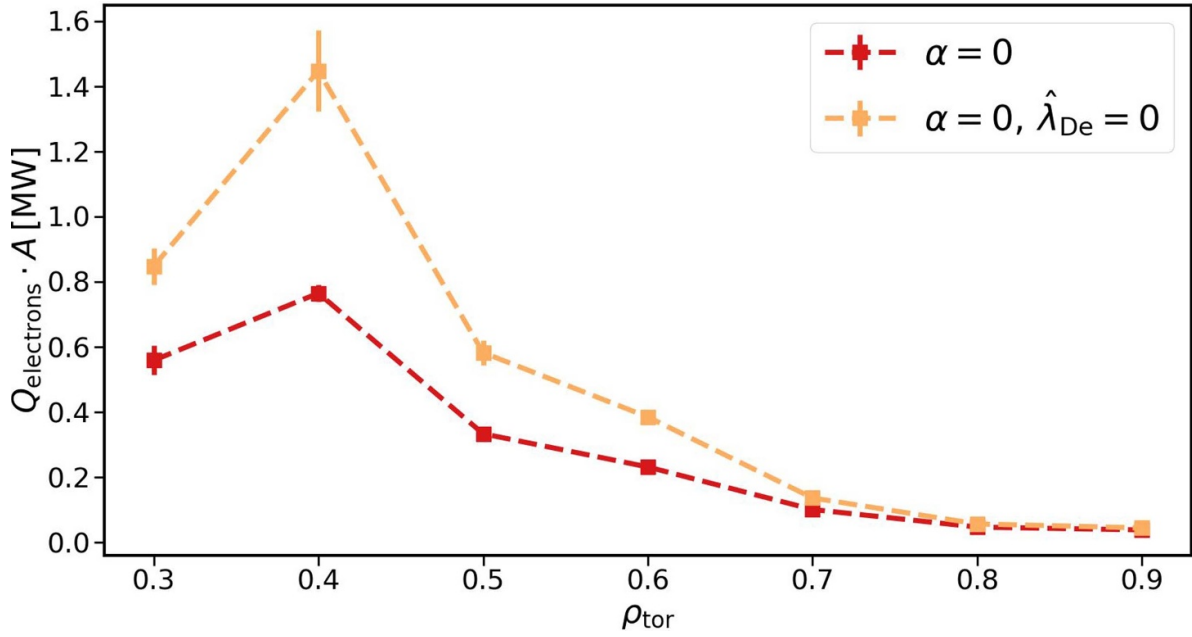


Figure 15. Radial electron-scale heat flux profiles of the $\alpha = 0$ -flux-tube with (red) and without (orange) including $\hat{\lambda}_{\text{De}}$.

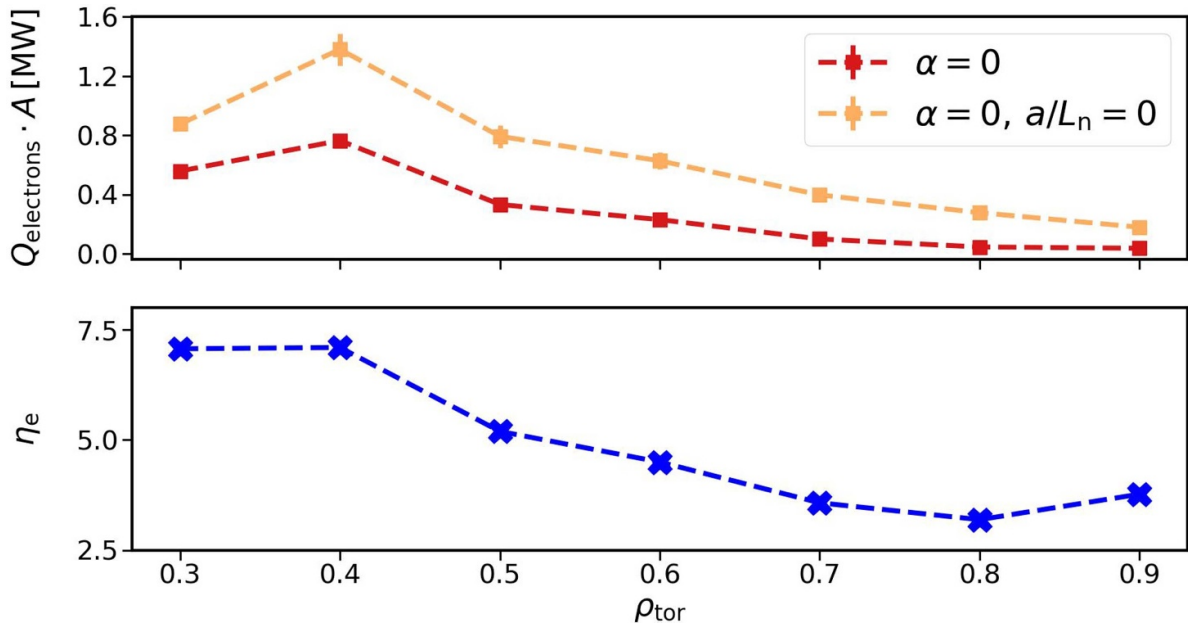


Figure 16. Top: radial electron-scale heat flux profiles of the $\alpha = 0$ -flux-tube with finite a/L_n (red) and with $a/L_n = 0$ (orange); bottom: radial variation of the normalised gradient ratio η_e .

6. Assessment of the particle flux

While we have presented a first-of-its-kind simulation of experimentally relevant parameters of a gas-fuelled ECRH discharge in W7-X, it is reasonable to question the validity of the conclusions drawn. This scepticism is justified as the simulated heat fluxes still fail to agree with the power balance predictions, even with the additional electron-scale contributions. Particularly, establishing a correlation between simulation and experiment for the outer region beyond $\rho_{\text{tor}} = 0.5$ is challenging due to the overestimation observed in the ion

heat flux calculated by GENE-3D. A more robust approach would involve a comprehensive coupling of several codes, such as GENE-3D, GENE (for ETG simulations), a neoclassical solver like KNOSOS [38], and other codes, to a transport code like Tango [39–41], in order to iteratively evolve the background profiles self-consistently until agreement with power balance is reached. While such an approach is routinely done for tokamaks [42, 43] already, it is only done globally using an adiabatic electron model [19] or within a FT framework with kinetic electrons [44] for stellarator geometries. Expanding the GENE-3D-Tango methodology to incorporate

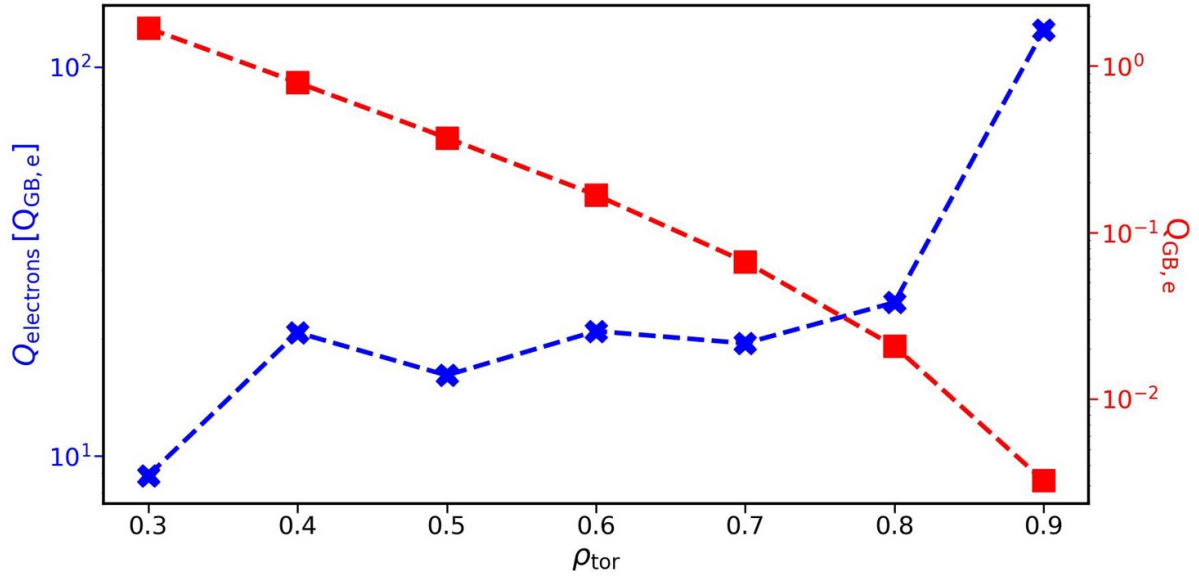


Figure 17. Blue: radial electron-scale heat flux profile in Gyrobohm units, averaged over all field lines considered, using nominal simulation parameters; red: radial variation of Gyrobohm transport. The subscript ‘e’ indicates that the electron mass was used as reference mass m_{ref} .

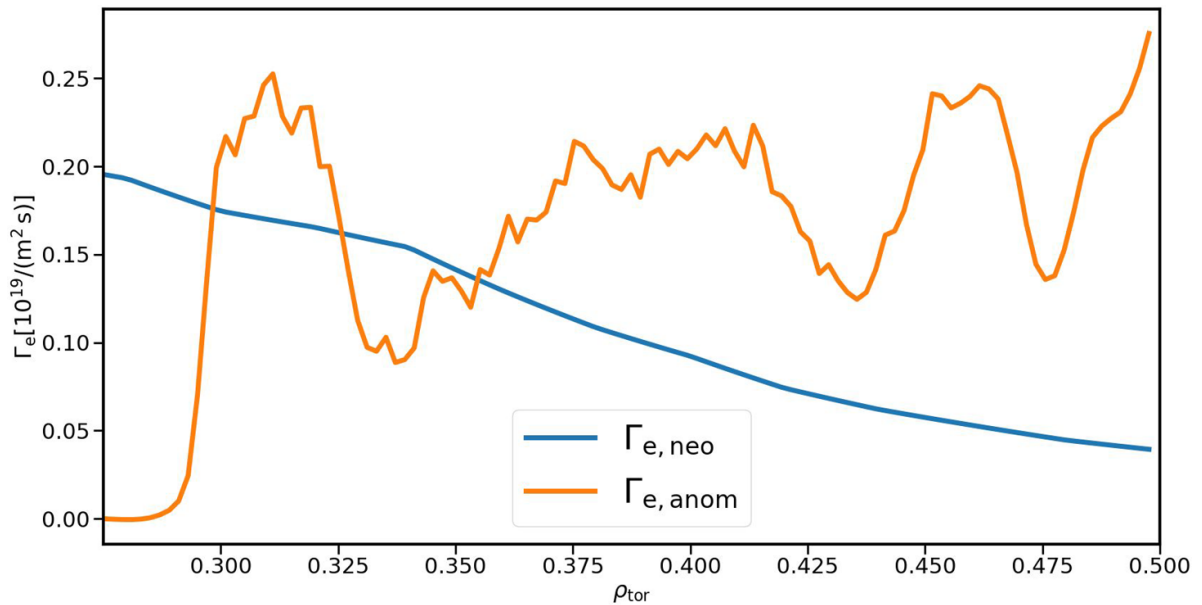


Figure 18. Radial profiles of contributions to the electron particle flux. The neoclassical particle flux, calculated with DKES, is shown in blue. In contrast, the anomalous flux, calculated with GENE-3D, is shown in orange.

kinetic electrons currently exceeds the scope of this paper but remains a target for the future.

Nevertheless, we can further strengthen the argument for the importance of TEM and ETG turbulence in the core of gas-fuelled ECRH plasmas without matching power balance by examining the individual contributions to the electron particle flux. While the experimental flux value remains unknown due to significant systematic uncertainties, it is plausible to assume that, for a purely gas-fuelled discharge, the total particle flux will tend towards zero or, at least, be very close to it deep within the plasma core. A qualitative assessment of the particle flux levels depicted in figure 18, when compared with findings from [15], suggests that the anomalous particle flux predicted

by GENE-3D appears too positive to align with the experiment. Typically, neoclassical transport is directed outward [45, 46], necessitating an inward turbulent particle flux when approaching the magnetic axis, a trend not observed here. Additionally, as highlighted in [15], an inward anomalous particle flux can be achieved by reducing the density gradient, increasing the ETG, or a combination of both. Considering that these adjustments would further increase the drive for ∇T_e -TEM and ETG turbulence, it stands to reason that when matching experimental heat and particle fluxes, the contributions of electron-induced turbulence to the electron heat flux would likely be even more pronounced than under the nominal profiles used in this analysis.

In summary, our findings provide robust evidence for the presence of trapped-electron turbulence within the core of gas-fuelled ECRH discharges, manifested in the form of ITG-TEM hybrids and ETG turbulence. Their relevance in high-performance discharges, such as those employing pellet fuelling, remains an avenue yet to be explored.

7. Conclusions

This paper delves into plasma turbulence analysis in an experimental ECRH discharge of W7-X using GENE-3D and GENE. Our study unveils that while FT and FFS simulations reasonably approximate the heat flux levels predicted by radially global simulations within the plasma core, they significantly overestimate transport in the outer plasma region. However, factoring in the shearing of external ExB-flow helps mitigate this discrepancy to some extent, underscoring its pivotal role in stabilising turbulence, even in standard stellarator discharges.

Moreover, we have provided substantial evidence supporting the existence of TEM turbulence within the plasma core, challenging previous notions proposed in existing literature [2, 11]. Although not solely accountable for transport, these modes were distinctly evident in the form of ITG-TEM hybrids, predominantly driven by the ETG.

Additionally, our study demonstrates, within our specific case, the substantial contribution of electron-scale simulations to electron heat flux in contrast to the suggestion of weak ETGs in W7-X outlined in [6]. We observed a diminishing impact of these modes in the plasma's outer radial region, attributed to the normalised ETG transport not increasing rapidly enough towards the edge to offset the decrease in the Gyrobohm scaling factor resulting from lower electron temperature and density.

Finally, we support the validity of our findings despite not aligning with transport predictions from power balance analysis. We assert that the impact of electron-induced turbulence is expected to significantly increase if background profiles are modulated to achieve experimentally realistic heat and particle fluxes.

In the future, we will extend these studies to a broader range of experimental discharge in order to generalise our claims, while additionally coupling GENE-3D simulations to the transport code Tango as shown in [19, 47] in order to achieve flux matching with the experiment. In addition, global simulations offer a direct comparison with turbulent fluctuation measurements via synthetic diagnostics [48] in order to identify signals of TEM in experimental discharges.

Acknowledgments

F. Wilms would like to thank G. Merlo and A. Di Siena for many fruitful insights and discussions. This work has been carried out within the framework of the EUROfusion Consortium, funded by the European Union via the Euratom Research and Training Programme (Grant Agreement No. 101052200—EURO-fusion). Views and opinions expressed are however

those of the author(s) only and do not necessarily reflect those of the European Union or the European Commission. Neither the European Union nor the European Commission can be held responsible for them. Numerical simulations were performed at the Cobra and Raven HPC system at the Max Planck Computing and Data Facility (MPCDF), Germany and the Marconi Fusion supercomputer at CINECA, Italy.

ORCID iDs

Felix Wilms  <https://orcid.org/0000-0001-9859-7420>
 Alejandro Bañón Navarro  <https://orcid.org/0000-0003-0487-6395>
 Sergey Bozhenkov  <https://orcid.org/0000-0003-4289-3532>
 Felix Warmer  <https://orcid.org/0000-0001-9585-5201>
 Daihong Zhang  <https://orcid.org/0000-0002-5800-4907>
 Frank Jenko  <https://orcid.org/0000-0001-6686-1469>

References

- [1] Beidler C.D. *et al* 2021 Demonstration of reduced neoclassical energy transport in Wendelstein 7-X *Nature* **596** 221–6
- [2] Klinger T. *et al* 2019 Overview of first Wendelstein 7-X high-performance operation *Nucl. Fusion* **59** 112004
- [3] Aleynikova K., Zocco A., Xanthopoulos P., Helander P. and Nührenberg C. 2018 Kinetic ballooning modes in tokamaks and stellarators *J. Plasma Phys.* **84** 745840602
- [4] Mishchenko A., Borchardt M., Hatzky R., Kleiber R., Könies A., Nührenberg C., Xanthopoulos P., Roberg-Clark G. and Plunk G.G. 2023 Global gyrokinetic simulations of electromagnetic turbulence in stellarator plasmas *J. Plasma Phys.* **89** 955890304
- [5] Jenko F. and Kendl A. 2002 Stellarator turbulence at electron gyroradius scales *New J. Phys.* **4** 35
- [6] Plunk G.G. *et al* 2019 Stellarators resist turbulent transport on the electron Larmor scale *Phys. Rev. Lett.* **122** 035002
- [7] Weir G.M. *et al* 2021 Heat pulse propagation and anomalous electron heat transport measurements on the optimized stellarator W7-X *Nucl. Fusion* **61** 056001
- [8] Proll J.H.E., Plunk G.G., Faber B.J., Görler T., Helander P., McKinney I.J., Poeschel M.J., Smith H.M. and Xanthopoulos P. 2022 Turbulence mitigation in maximum-J stellarators with electron-density gradient *J. Plasma Phys.* **88** 905880112
- [9] Xanthopoulos P. *et al* (The W7-X Team) 2020 Turbulence mechanisms of enhanced performance stellarator plasmas *Phys. Rev. Lett.* **125** 075001
- [10] Alcusón J.A., Xanthopoulos P., Plunk G.G., Helander P., Wilms F., Turkin Y., Von Stechow A. and Grulke O. 2020 Suppression of electrostatic micro-instabilities in maximum-J stellarators *Plasma Phys. Control. Fusion* **62** 035005
- [11] Grulke O. *et al* 2018 Plasma dynamics and transport studies in Wendelstein 7-X *27th IAEA Fusion Energy Conf. (FEC 2018) (Gandhinagar, India, 22–27 October 2018)* (available at: https://inis.iaea.org/collection/NCLCollectionStore/_Public/50/050/50050305.pdf?r=1)
- [12] Warmer F. *et al* 2021 Impact of magnetic field configuration on heat transport in stellarators and heliotrons *Phys. Rev. Lett.* **127** 225001
- [13] Estrada T. *et al* 2021 Radial electric field and density fluctuations measured by Doppler reflectometry during the

- post-pellet enhanced confinement phase in W7-X *Nucl. Fusion* **61** 046008
- [14] Zhang D. *et al* 2023 Observation of impurity accumulation and its compatibility with high plasma performance in W7-X *Plasma Phys. Control. Fusion* **65** 105006
- [15] Thienpondt H. *et al* 2023 Prevention of core particle depletion in stellarators by turbulence *Phys. Rev. Res.* **5** L022053
- [16] Wilms F., Bañón Navarro A., Merlo G., Leppin L., Görler T., Dannert T., Hindenlang F. and Jenko F. 2021 Global electromagnetic turbulence simulations of W7-X-like plasmas with GENE-3D *J. Plasma Phys.* **87** 905870604
- [17] Mishchenko A. *et al* 2022 Gyrokinetic particle-in-cell simulations of electromagnetic turbulence in the presence of fast particles and global modes *Plasma Phys. Control. Fusion* **64** 104009
- [18] Singh T., Nicolau J.H., Lin Z., Sharma S., Sen A. and Kulev A. 2022 Global gyrokinetic simulations of electrostatic microturbulent transport using kinetic electrons in LHD stellarator *Nucl. Fusion* **62** 126006
- [19] Bañón Navarro A., Di Siena A., Velasco J.L., Wilms F., Merlo G., Windisch T., LoDestro L.L., Parker J.B. and Jenko F. 2023 First-principles based plasma profile predictions for optimized stellarators *Nucl. Fusion* **63** 054003
- [20] Cole M.D.J., Moritaka T., Hager R., Dominski J., Ku S. and Chang C.S. 2020 Nonlinear global gyrokinetic delta-*f* turbulence simulations in a quasi-axisymmetric stellarator *Phys. Plasmas* **27** 044501
- [21] Maurer M., Bañón Navarro A., Dannert T., Restelli M., Hindenlang F., Görler T., Told D., Jarema D., Merlo G. and Jenko F. 2020 GENE-3D: a global gyrokinetic turbulence code for stellarators *J. Comput. Phys.* **420** 109694
- [22] Proll J.H.E., Mynick H.E., Xanthopoulos P., Lazerson S.A. and Faber B.J. 2015 TEM turbulence optimisation in stellarators *Plasma Phys. Control. Fusion* **58** 014006
- [23] Stroteich S., Xanthopoulos P., Plunk G. and Schneider R. 2022 Seeking turbulence optimized configurations for the Wendelstein 7-X stellarator: ion temperature gradient and electron temperature gradient turbulence *J. Plasma Phys.* **88** 175880501
- [24] Van Rij W.I. and Hirshman S.P. 1989 Variational bounds for transport coefficients in three-dimensional toroidal plasmas *Phys. Fluids B* **1** 563–9
- [25] Jenko F., Dorland W., Kotschenreuther M. and Rogers B.N. 2000 Electron temperature gradient driven turbulence *Phys. Plasmas* **7** 1904–10
- [26] Görler T., Lapillonne X., Brunner S., Dannert T., Jenko F., Merz F. and Told D. 2011 The global version of the gyrokinetic turbulence code GENE *J. Comput. Phys.* **230** 7053–71
- [27] Li M., Breizman B.N. and Zheng L. 2016 Canonical straight field line magnetic flux coordinates for tokamaks *J. Comput. Phys.* **326** 334–41
- [28] Martin M.F., Landreman M., Xanthopoulos P., Mandell N.R. and Dorland W. 2018 The parallel boundary condition for turbulence simulations in low magnetic shear devices *Plasma Phys. Control. Fusion* **60** 095008
- [29] Turkin Y., Maaßberg H., Beidler C.D., Geiger J. and Marushchenko N.B. 2006 Current control by ECCD for W7-X *Fusion Sci. Technol.* **50** 387–94
- [30] Kotschenreuther M. *et al* 2019 Gyrokinetic analysis and simulation of pedestals to identify the culprits for energy losses using ‘fingerprints’ *Nucl. Fusion* **59** 096001
- [31] Proll J.H.E., Xanthopoulos P. and Helander P. 2013 Collisionless microinstabilities in stellarators. II. Numerical simulations *Phys. Plasmas* **20** 122506
- [32] Plunk G.G., Helander P., Xanthopoulos P. and Connor J.W. 2014 Collisionless microinstabilities in stellarators. III. The ion-temperature-gradient mode *Phys. Plasmas* **21** 032112
- [33] Banón Navarro A., Morel P., Albrecht-Marc M., Carati D., Merz F., Görler T. and Jenko F. 2011 Free energy cascade in gyrokinetic turbulence *Phys. Rev. Lett.* **106** 055001
- [34] Plunk G.G., Connor J.W. and Helander P. 2017 Collisionless microinstabilities in stellarators. Part 4. The ion-driven trapped-electron mode *J. Plasma Phys.* **83** 715830404
- [35] Xanthopoulos P. and Jenko F. 2007 Gyrokinetic analysis of linear microinstabilities for the stellarator Wendelstein 7-X *Phys. Plasmas* **14** 042501
- [36] Alcusón J.A. *et al* 2023 Quantitative comparison of impurity transport in turbulence reduced and enhanced scenarios at Wendelstein 7-X *Nucl. Fusion* **63** 094002
- [37] Proll J.H.E., Helander P., William Connor J. and Plunk G.G. 2012 Resilience of quasi-isodynamic stellarators against trapped-particle instabilities *Phys. Rev. Lett.* **108** 245002
- [38] Velasco J.L., Calvo I., Parra F.I. and García-Regaña J.M. 2020 KNOSOS: a fast orbit-averaging neoclassical code for stellarator geometry *J. Comput. Phys.* **418** 109512
- [39] Parker J.B., LoDestro L.L., Told D., Merlo G., Ricketson L.F., Campos A., Jenko F. and Hittinger J.A.F. 2018 Bringing global gyrokinetic turbulence simulations to the transport timescale using a multiscale approach *Nucl. Fusion* **58** 054004
- [40] Parker J.B., LoDestro L.L. and Campos A. 2018 Investigation of a multiple-timescale turbulence-transport coupling method in the presence of random fluctuations *Plasma* **1** 126–43
- [41] Shestakov A.I., Cohen R.H., Crotinger J.A., LoDestro L.L., Tarditi A. and Xu X.Q. 2003 Self-consistent modeling of turbulence and transport *J. Comput. Phys.* **185** 399–426
- [42] Di Siena A. *et al* 2022 Global gyrokinetic simulations of ASDEX Upgrade up to the transport timescale with GENE-Tango *Nucl. Fusion* **62** 106025
- [43] Di Siena A. *et al* 2023 Predictions of improved confinement in sparc via energetic particle turbulence stabilization *Nucl. Fusion* **63** 036003
- [44] Mandell N., Dorland W., Parra F., Qian T., Sachdev J. and Luis Velasco J. 2023 Stellarator profile prediction and evolution using the Trinity3D+ GX+ KNOSOS multi-scale gyrokinetic framework *Bull. Am. Phys. Soc.* **2023** U006–011
- [45] Maaßberg H., Beidler C.D. and Simmet E.E. 1999 Density control problems in large stellarators with neoclassical transport *Plasma Phys. Control. Fusion* **41** 1135
- [46] Beidler C.D., Feng Y., Geiger J., Köchl F., Maßberg H., Marushchenko N.B., Nührenberg C., Smith H.M. and Turkin Y. 2018 (Expected difficulties with) density-profile control in W7-X high-performance plasmas *Plasma Phys. Control. Fusion* **60** 105008
- [47] Bañón Navarro A., Roberg-Clark G.T., Plunk G.G., Fernando D., Di Siena A., Wilms F. and Jenko F. 2023 Assessing global ion thermal confinement in critical-gradient-optimized stellarators (arXiv:2310.18705)
- [48] Hansen S.K. *et al* 2022 Development of a synthetic phase contrast imaging diagnostic for turbulence studies at Wendelstein 7-X *Plasma Phys. Control. Fusion* **64** 095011